Theoretical study of structural, electronic, and optical properties of ternary metal sulfides $M\mathrm{BiS}_2$ (M=Ag, Na)

Shugo Suzuki∗ and Makoto Tsuyama

Division of Materials Science, Faculty of Pure and Applied Sciences, University of Tsukuba,

Tsukuba, Ibaraki 305-8573, Japan

We study the structural, electronic, and optical properties of $M\mathrm{BiS}_2$ (M=Ag, Na) using the relativistic all-electron calculations. We find that for both M=Ag and Na, the $R\bar{3}m$ and $Fd\bar{3}m$ superstructures are the lowest-energy superstructures. $R\bar{3}m$ and $Fd\bar{3}m$ $M\mathrm{BiS}_2$ are indirect-band-gap semiconductors with the differences between the indirect and direct band gaps, Δ, of about 0.5 and 0.1 eV for M=Ag and Na, respectively. $R\bar{3}m$ and $Fd\bar{3}m$ $M\mathrm{BiS}_2$ exhibit high absorption coefficients of the order of 10^5 cm^{-1}. Employing the spectroscopically limited maximum efficiency as a metric for quantifying the photovoltaic performance, it is found that the power conversion efficiency in the thick-film limit for M=Na is 32% because of its small Δ while that for M=Ag is 15% because of its large Δ.

1. Introduction

Over the last few decades, metal chalcogenides have received considerable attention for applications in photovoltaic technologies. In particular, CdTe and $\mathrm{CuIn}_x\mathrm{Ga}_{1-x}\mathrm{Se}_2$ (CIGS) are two successful photovoltaic materials widely used in commercialized thin-film solar cells.[1,2] Their main advantages are high power conversion efficiencies (PCE) of over 20%, long-term stability, low fabrication costs, and short energy payback time. On the other hand, however, there remain issues to be addressed; they contain toxic elements such as Cd or scarce elements such as Te or In. Accordingly, it is highly desirable to search for alternative absorber materials with non-toxic and earth-abundant elements.

To address the toxicity and scarcity issues, significant efforts have been made to find alternative metal chalcogenides during the last decade. In particular, $\mathrm{Cu}_2\mathrm{ZnSnS}_4$ (CZTS) and related compounds have been shown to be promising absorber materials composed of non-toxic and earth-abundant elements;[3–9] the electronic and optical properties of CZTS are similar to those of CIGS and well suited for use as absorber materials in thin-film solar cells. Also, $\mathrm{Sn}X$, Sb_2X_3, Bi_2X_3, and $\mathrm{CuSb}X_2$ (X=S, Se) have been investigated as promising candidates for absorber materials composed of non-toxic and earth-abundant elements, and considerable efforts have been devoted to the development of thin-film solar cells based on

these materials.[10–25]

Recently, a ternary metal sulfide $AgBiS_2$ has drawn much interest for photovoltaic applications.[26–48] Bernechea et al. reported a certified PCE of 6.3% using ultrathin-film colloidal-nanocrystal solar cells based on $AgBiS_2$ nanocrystals.[31] $AgBiS_2$ is not only non-toxic and earth-abundant but also low-temperature solution processable.[26–31,35–41] It has also been reported that the devices based on $AgBiS_2$ are highly stable without encapsulation under ambient conditions.[31,36,41] The measured band gap for bulk $AgBiS_2$ is 0.9 eV while that for $AgBiS_2$ nanocrystals is 1.0 to 1.4 eV;[26–31,33,34,36–39] the increase in the band gap for $AgBiS_2$ nanocrystals is considered to be due to the quantum confinement effect. Furthermore, the $AgBiS_2$ thin films exhibit very high absorption coefficient of the order of 10^5 cm^{-1}.[31,37,40]

At room temperature, bulk $AgBiS_2$ crystallizes in an ordered hexagonal structure with the space group $P\bar{3}m1$, while it transforms into a disordered cubic structure with the space group $Fm\bar{3}m$ above 468 K.[49–55] Both the ordered hexagonal and disordered cubic structures are based on the NaCl-type structure. In these structures, the S atoms occupy the anion sublattice. On the other hand, in the ordered hexagonal structure, the Ag and Bi atoms alternately occupy the (111) layers in the cation sublattice while in the disordered cubic structure, the Ag and Bi atoms occupy the cation sublattice indistinguishably. It is worth mentioning that the ordered hexagonal phase of $AgBiS_2$ is extremely difficult to obtain because it requires annealing process for more than two weeks.[49,52] This may be one of the main reasons why $AgBiS_2$ nanocrystals exhibit the disordered cubic structure.[26–41] The disordered cubic phase of $AgBiS_2$ is a consequence of various local superstructures. In the previous theoretical study by Hoang et al. for the closely related ternary chalcogenides $AgSbX_2$ (X=S, Se, Te), the relative stability of four superstructures, which are associated with the space groups $R\bar{3}m$, $Fd\bar{3}m$, $I4_1/amd$, and $P4/mmm$, has been investigated.[56,57] They found that among the four superstructures, the $R\bar{3}m$ and $Fd\bar{3}m$ superstructures are the lowest-energy superstructures. For $AgBiS_2$, however, although the previous theoretical studies investigated the structural, electronic, and optical properties of some of the four possible superstructures,[42–48] there are few systematic theoretical studies of the properties of its possible superstructures.

Furthermore, another ternary metal sulfide $NaBiS_2$ has also received considerable attention in recent years.[58–66] Although the previous studies have mainly focused on its photocatalytic properties, $NaBiS_2$ is also a promising candidate for photovoltaic applications because its structural, electronic, and optical properties are similar to those of $AgBiS_2$. $NaBiS_2$, like $AgBiS_2$, crystallizes in the disordered cubic structure of NaCl type.[67] The measured band gap of 1.1 to 1.4 eV falls within the ideal range for photovoltaic applications.[59–65] As mentioned

above, the disordered cubic phase is a consequence of various local superstructures.[56,57] Rosales et al. studied the relative stability of possible superstructures of NaBiS$_2$ based on the density functional theory and found that the $R\bar{3}m$ and $Fd\bar{3}m$ superstructures are the lowest-energy superstructures.[60] These results provide important insights into the structural properties of NaBiS$_2$. However, there are no thorough theoretical studies of the electronic and optical properties of the superstructures. Therefore, when considering photocatalytic and photovoltaic applications, it is still desirable to investigate their electronic and optical properties more in detail.

In this work, we study the structural, electronic, and optical properties of possible superstructures of MBiS$_2$ (M=Ag, Na) using the relativistic all-electron calculations based on the density functional theory. In particular, we carry out fully relativistic calculations of their electronic structures and absorption coefficients using four-component spinors obtained as the solutions of the Dirac-Kohn-Sham equations, which may be important because MBiS$_2$ contain heavy element Bi. Using the calculated absorption coefficients, we estimate the PCE of MBiS$_2$ employing the spectroscopically limited maximum efficiency as a metric for quantifying the photovoltaic performance. The method of calculations is explained in Sect. 2. The results and discussion are given in Sect. 3. Finally, we give the conclusions of this work in Sect. 4.

2. Method of calculations

The local superstructures for the disordered cubic phase of MBiS$_2$ considered in this work are those with the space groups of $R\bar{3}m$, $Fd\bar{3}m$, $I4_1/amd$, and $P4/mmm$.[56,57] These superstructures are based on the NaCl-type structure. In Fig. 1, we show their schematic diagrams depicted using VESTA.[68] For each of $R\bar{3}m$, $I4_1/amd$, and $P4/mmm$ MBiS$_2$, the left diagram is the 2×2×2 cubic supercell containing eight NaCl-type unit cells while the right diagram is its conventional unit cell. For $Fd\bar{3}m$ MBiS$_2$, on the other hand, only one diagram is shown because its conventional unit cell is identical to the cubic supercell. We refer to the three directions along the edges of the cubic supercell as the x, y, and z directions as shown in Fig. 1. The primitive unit cells of $R\bar{3}m$, $Fd\bar{3}m$, $I4_1/amd$, and $P4/mmm$ MBiS$_2$ contain 4, 16, 8, and 4 atoms, respectively. In all the superstructures, the S atoms occupy the anion sublattice. The arrangements of the M and Bi atoms in the cation sublattice in these superstructures are as follows. The cation arrangement in $R\bar{3}m$ MBiS$_2$ is characterized by the stacking sequence of alternating M and Bi layers with (111) orientation. The $Fd\bar{3}m$ superstructure is obtained by rotating every other (001) layer in the $R\bar{3}m$ superstructure by 90° around the z axis. The

$I4_1/amd$ superstructure consists of the square-lattice $M\mathrm{BiS_2}$ layers with (001) orientation, which are stacked in the z direction so as to form a body-centered tetragonal lattice. The cation arrangement in the $P4/mmm$ superstructure is characterized by the stacking sequence of alternating M and Bi layers with (001) orientation. The common feature of the the $R\bar{3}m$ and $Fd\bar{3}m$ superstructures is the existence of the M-S-Bi-S chains along the x, y, and z directions. In the $I4_1/amd$ superstructure, there exist the M-S-M-S and Bi-S-Bi-S chains along the x and y directions together with the M-S-Bi-S chains along the z direction. In the $P4/mmm$ superstructure, only the M-S-M-S and Bi-S-Bi-S chains exist along the x, y, and z directions, but M-S-Bi-S chains are absent. It is also worth noting that the S atoms in the $R\bar{3}m$, $Fd\bar{3}m$, and $I4_1/amd$ superstructures are octahedrally coordinated by three M and three Bi atoms while the S atoms in the $P4/mmm$ superstructure are octahedrally coordinated by two M and four Bi atoms or by four M and two Bi atoms.
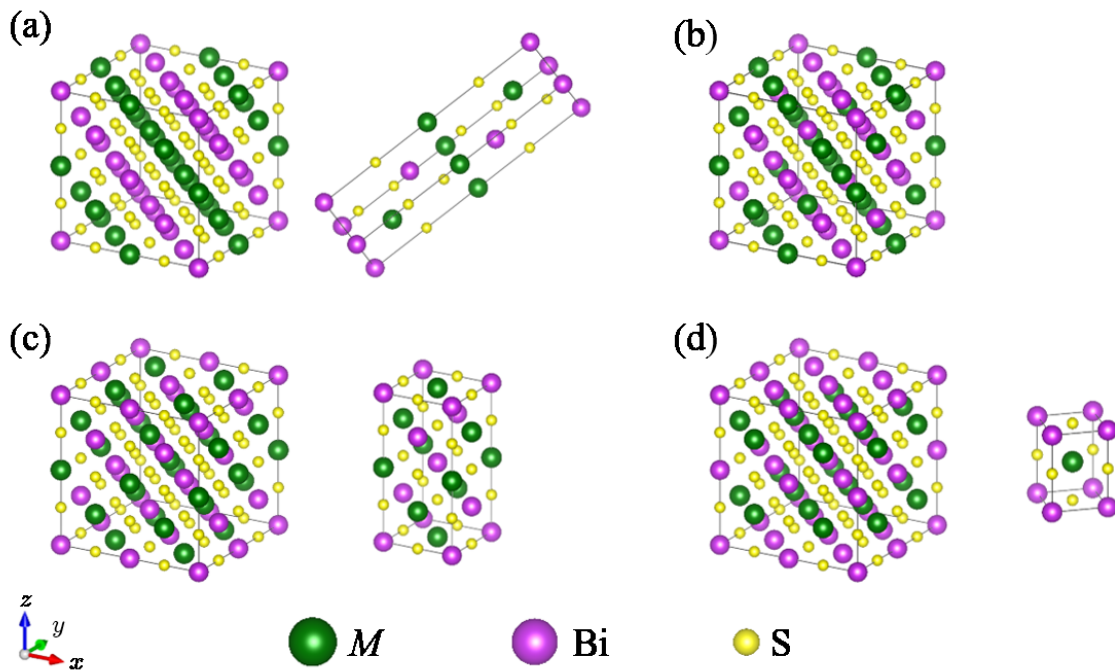

Fig. 1. (Color online) Schematic diagrams for the (a) $R\bar{3}m$, (b) $Fd\bar{3}m$, (c) $I4_1/amd$, and (d) $P4/mmm$ superstructures of $M\mathrm{BiS_2}$. For each of the $R\bar{3}m$, $I4_1/amd$, and $P4/mmm$ superstructures, the left diagram is the 2×2×2 cubic supercell containing eight NaCl-type unit cells while the right diagram is its conventional unit cell. For the $Fd\bar{3}m$ superstructure, only one diagram is shown because its conventional unit cell is identical to the cubic supercell.

We carried out all-electron calculations based on the density functional theory.[69–75] The generalized gradient approximation (GGA) to the exchange-correlation energy func-

tional was adopted using the Perdew-Burke-Ernzerhof form.[76] The lattice constants and the atomic positions were optimized with the scalar relativistic full-potential linear-combination-of-atomic-orbitals (SFLCAO) method.[71] Using the optimized structures, the band structures, the densities of states, and the absorption coefficients were calculated with the fully relativistic full-potential linear-combination-of-atomic-orbitals (FFLCAO) method.[70,72]

The absorption coefficients were obtained from the optical conductivity calculated within the independent particle approximation combined with a phenomenological approach.[72–75] The optical transition matrix elements were calculated using the four-component spinors obtained as the solutions of the Dirac-Kohn-Sham equations to take into account all the relativistic effects including spin-orbit coupling (SOC). Also, the phenomenological relaxation-time parameter $\hbar/\tau$ was used to simulate the lifetime of excitations; for all the materials studied in this work, $\hbar/\tau = 0.3$ eV was used.

Using the calculated absorption coefficients, we evaluated the PCE employing the spectroscopically limited maximum efficiency (SLME) as a metric for quantifying the photovoltaic performance.[77] The SLME is a generalization of the Shockley-Queisser limit.[78] One important feature of the SLME is that for a material whose fundamental band gap is indirect, the SLME takes into account the non-radiative recombination by considering $\Delta = E_{\mathrm{g}}^{\mathrm{da}} - E_{\mathrm{g}}$, where E_{g} and $E_{\mathrm{g}}^{\mathrm{da}}$ are the fundamental and direct allowed band gaps, respectively. Also, another important point is that the SLME considers the material-dependent absorption coefficient in the expression $a(E) = 1 - e^{-2\alpha(E)L}$, where $a(E)$, $\alpha(E)$, and L are the absorptivity, the absorption coefficient, and the film thickness, respectively. Note that the SLME is sensitive to $\alpha(E)$ because $a(E)$ depends exponentially on $\alpha(E)$. In calculating the SLME, the standard AM1.5G solar spectrum is used.[79] The atomic orbitals used as the basis functions are as follows: the $1s$, $2s$, $2p$, $3s$, $3p$, $3d$, $4s$, $4p$, $4d$, $5s$ orbitals of the neutral Ag atom; the $5s$, $5p$ orbitals of the Ag^{2+} atom; the $4d$ orbitals of the Ag^{4+} atom; the $1s$, $2s$, $2p$, $3s$ orbitals of the neutral Na atom; the $3s$, $3p$, $3d$ orbitals of the Na^{2+} atom; the $1s$, $2s$, $2p$, $3s$, $3p$, $3d$, $4s$, $4p$, $4d$, $4f$, $5s$, $5p$, $5d$, $6s$, $6p$ orbitals of the neutral Bi atom; the $6s$, $6p$, $6d$ orbitals of the Bi^{2+} atom; the $1s$, $2s$, $2p$, $3s$, $3p$ orbitals of the neutral S atom; the $3s$, $3p$, $3d$ orbitals of the S^{2+} atom. It is worth noting that the use of the atomic orbitals of positively charged atoms along with those of neutral atoms is crucial to describing the contraction of atomic orbitals associated with cohesion. The Brillouin zone sampling for the structure optimization was performed using a $4 \times 4 \times 4$ $\boldsymbol{k}$ point grid for the $Fd\bar{3}m$ and $I4_1/amd$ superstructures while using 185 $\boldsymbol{k}$ points generated with the good-lattice-point method for the $R\bar{3}m$ and $P4/mmm$ superstructures because of the relatively small number of atoms in their unit cells.[80,81] We used the force criterion of 0.01

eV/Å to stop the optimization of the atomic positions. We used 185 k points generated with the good-lattice-point method for calculating the self-consistent potential. We used several sets of k points generated with the good-lattice-point method for calculating the absorption coefficients, increasing the number of k points from 185 to 4044 until converged results were obtained. The band structure of MBiS$_2$ for each superstructure was calculated along the path connecting the symmetry points in the Brillouin zone given by Hinuma et al.[82]

3.   Results and discussion

In Table I, for $R\bar{3}m$, $Fd\bar{3}m$, $I4_1/amd$, and $P4/mmm$ MBiS$_2$, we show the optimized lattice constants, a and c, the M-S and Bi-S distances, and the total energies relative to the lowest-energy superstructure, ΔE. The experimental lattice constants of the disordered cubic structures are also shown. The value in the parenthesis immediately after each of a and c is the corresponding lattice constant of the ideal NaCl-type cubic structure, a_0, which is given as follows: $\sqrt{2}a$ and $\sqrt{3}c/6$ for $R\bar{3}m$, $a/2$ for $Fd\bar{3}m$, a and $c/2$ for $I4_1/amd$, $\sqrt{2}a/2$ and c for $P4/mmm$. The relative total energies ΔE shown in the table are given in units of meV per formula unit and calculated using both the FFLCAO method (with SOC) and the SFLCAO method (without SOC) adopting the structure optimized with the SFLCAO method.

The differences between the calculated a_0 and the experimental lattice constants of the disordered cubic phase are in the range of 1-3%. Also, the calculated Ag-S and Bi-S distances are in the range of 2.8-2.9 Å, which is consistent with the experimentally measured ones for the ordered hexagonal phase of AgBiS$_2$: 2.74-2.78 Å for the Ag-S distance and 2.90-2.95 Å for the Bi-S distance.[49] Thus, as far as only the structures are concerned, all of $R\bar{3}m$, $Fd\bar{3}m$, $I4_1/amd$, and $P4/mmm$ MBiS$_2$ seem possible as the local superstructures for the disordered cubic phase. However, the relative total energies ΔE listed in Table I show that the lowest-energy superstructures are $R\bar{3}m$ and $Fd\bar{3}m$ for both AgBiS$_2$ and NaBiS$_2$. The differences between the total energies of these two lowest-energy superstructures are considerably small, less than 8 meV/f.u., regardless of whether or not SOC is considered. On the other hand, ΔE of $I4_1/amd$ and $P4/mmm$ MBiS$_2$ are much larger for both M=Ag and Na; ΔE of $I4_1/amd$ and $P4/mmm$ AgBiS$_2$ are about 160 and 380 meV/f.u., respectively, and those of $I4_1/amd$ and $P4/mmm$ NaBiS$_2$ are about 150 and 440 meV/f.u., respectively. Thus, it is most likely that the disordered cubic phase observed in the previous experimental studies is dominated by the local superstructures with the atomic arrangements found in $R\bar{3}m$ and $Fd\bar{3}m$ MBiS$_2$. These results are consistent with those reported in the previous theoretical study of closely related ternary chalcogenides AgSbX (X=S, Se, Te),[56] Also, the above result obtained for

$NaBiS_2$ is consistent with the result reported by Rosales et al. that the total energies of $R\bar{3}m$ and $Fd\bar{3}m$ $NaBiS_2$ are almost the same but lower than that of $I4_1/amd$ $NaBiS_2$.[60]

The ordered hexagonal structure of $AgBiS_2$ observed at room temperature in the previous experimental studies is associated with the space group $P\bar{3}m1$;[49,52] it was shown that the structure of $P\bar{3}m1$ $AgBiS_2$ is slightly distorted from that of $R\bar{3}m$ $AgBiS_2$. To examine the differences between the properties of $P\bar{3}m1$ $AgBiS_2$ and those of $R\bar{3}m$ $AgBiS_2$, we also carried out the calculations for the structural properties of $P\bar{3}m1$ $AgBiS_2$, as well as its electronic and optical properties. We found that the optimized lattice constants and atomic positions of $P\bar{3}m1$ $AgBiS_2$ are very close to those of $R\bar{3}m$ $AgBiS_2$ in agreement with the experimental observation; a and c for $P\bar{3}m1$ $AgBiS_2$ are 4.05 and 19.48 Å, respectively, and the Ag-S and Bi-S distances are 2.80 and 2.89 Å, respectively. The calculated total energy of $P\bar{3}m1$ $AgBiS_2$ is slightly lower than that of $R\bar{3}m$ $AgBiS_2$, with a difference of about 12 meV/f.u. Although the difference is considerably small, $P\bar{3}m1$ $AgBiS_2$ is found to be the most stable among the $AgBiS_2$ systems studied in this work. This is in agreement with the experimental observation that $P\bar{3}m1$ $AgBiS_2$ is the most stable modification at lower temperatures.[49,52] Our calculated total energy of $P\bar{3}m1$ $AgBiS_2$ is lower by about 380 meV/f.u. than that of $P4/mmm$ $AgBiS_2$. This is in agreement with the result of the previous theoretical study reported by Viñes et al.;[42] they found that the total energy of $P\bar{3}m1$ $AgBiS_2$ is lower than that of $P4/mmm$ $AgBiS_2$ by about 400 meV/f.u.

We also found that the electronic and optical properties of $R\bar{3}m$ $AgBiS_2$ and those of $P\bar{3}m1$ $AgBiS_2$ are very similar due to the similarity between their structures mentioned above. For example, the difference between the calculated band gaps of $R\bar{3}m$ and $P\bar{3}m1$ $AgBiS_2$ is only 0.01 eV. For this reason, in the rest of this article, we will refer only to the results of calculations for the electronic and optical properties of $R\bar{3}m$ $AgBiS_2$, not to those for $P\bar{3}m1$ $AgBiS_2$. Note, however, that we will refer to the results reported in the previous theoretical studies for $P\bar{3}m1$ $AgBiS_2$ for comparison if necessary.[42,45,47]

We show the band structures and the densities of states of $R\bar{3}m$, $Fd\bar{3}m$, $I4_1/amd$, and $P4/mmm$ $MBiS_2$ calculated with the FFLCAO method in Figs. 2 and 3 for M=Ag and Na, respectively. In the figures, the conduction band minimum and the valence band maximum are shown by red and green circles, respectively.

It is found that all of $MBiS_2$ are semiconductors with indirect band gaps, except for $P4/mmm$ $AgBiS_2$, which is metallic in consistent with the results of the previous theoretical studies.[42,48] The indirect band gaps of $R\bar{3}m$, $Fd\bar{3}m$, and $I4_1/amd$ $AgBiS_2$ are 0.26, 0.46, and 0.05 eV, respectively, while those of $R\bar{3}m$, $Fd\bar{3}m$, $I4_1/amd$, and $P4/mmm$ $NaBiS_2$ are 0.92,

Table I. Optimized lattice constants a and c (in Å), the M-S and Bi-S distances (in Å), and the total energies relative to that of the lowest-energy superstructure ΔE (in meV/f.u.). The experimentally measured lattice constants of the disordered cubic structures are also shown. The value in the parenthesis immediately after each of a and c is the corresponding lattice constant of the ideal NaCl-type cubic structure (see main text for details).

Material	Superstructure	a (Å)	c (Å)	M-S (Å)	Bi-S (Å)	ΔE (meV/f.u.)	
						with SOC	without SOC
AgBiS$_2$	$R\bar{3}m$	4.03 (5.70)	19.52 (5.63)	2.80	2.88	8	5
	$Fd\bar{3}m$	11.39 (5.70)		2.80	2.89	0	0
	$I4_1/amd$	5.70 (5.70)	11.45 (5.73)	2.85, 2.86	2.85, 2.87	152	174
	$P4/mmm$	4.08 (5.77)	5.57 (5.57)	2.79, 2.89	2.79, 2.89	334	421
	Expt.	5.648[a]		2.74, 2.75, 2.78[a]	2.90, 2.91, 2.95[a]		
NaBiS$_2$	$R\bar{3}m$	4.08 (5.77)	20.50 (5.92)	2.92	2.89	0	0
	$Fd\bar{3}m$	11.63 (5.82)		2.92	2.89	2	0
	$I4_1/amd$	5.74 (5.74)	11.93 (5.97)	2.87, 3.09	2.87, 2.87	142	167
	$P4/mmm$	4.11 (5.81)	5.59 (5.59)	2.80, 2.91	2.80, 2.91	407	477
	Expt.	5.775[b]					

a) Ref. 49.　　b) Ref. 62.

1.23, 0.13, and 0.09 eV, respectively. The differences between the indirect and direct band gaps, Δ, of $R\bar{3}m$, $Fd\bar{3}m$, and $I4_1/amd$ AgBiS$_2$ are 0.58, 0.46, and 0.002 eV, respectively, while those of $R\bar{3}m$, $Fd\bar{3}m$, $I4_1/amd$, and $P4/mmm$ NaBiS$_2$ are 0.08, 0.15, 0.03, and 0.19 eV, respectively. The calculated densities of states of AgBiS$_2$ show that the conduction bands are dominated by the Bi $6p$ and S $3p$ orbitals while the valence bands by the S $3p$ and Ag $4d$ orbitals with a slight contribution from the Bi $6s$ and $6p$ orbitals. On the other hand, the densities of states of NaBiS$_2$ show that the conduction bands are also dominated by Bi $6p$ and S $3p$ orbitals while the valence bands by the S $3p$ with a slight contribution from the Bi $6s$ and $6p$ orbitals. In particular, for $R\bar{3}m$ and $Fd\bar{3}m$ NaBiS$_2$, the Bi $6s$ contribution is noticeable at the valence band edge.

The conduction bands of $R\bar{3}m$ and $Fd\bar{3}m$ MBiS$_2$ exhibit several common features. There exist well-separated three lowest conduction bands of $R\bar{3}m$ MBiS$_2$ consisting of Bi $6p$ and S $3p$ orbitals in the energy region from 0 to 4 eV. The clear separation of the three bands is a consequence of SOC, which is in agreement with the band structure of $P\bar{3}m1$ AgBiS$_2$ calculated with SOC reported by Tabeti et al.[47] These well-separated three bands for $R\bar{3}m$ MBiS$_2$ correspond to the three sets of fourfold bands for $Fd\bar{3}m$ MBiS$_2$ located in the same energy region, also consisting of Bi $6p$ and S $3p$ orbitals; the four times difference in the

number of bands is due to the difference in the number of atoms in the primitive unit cell. The correspondence mentioned above is recognizable in their densities of states for $R\bar{3}m$ and $Fd\bar{3}m$ AgBiS$_2$ with three distinct peaks although the three peak structure is not clear for NaBiS$_2$. On the contrary, the dispersion of the conduction bands for $I4_1/amd$ and $P4/mmm$ MBiS$_2$ is much larger than that for $R\bar{3}m$ and $Fd\bar{3}m$ MBiS$_2$, resulting in the reduction of the band gaps and the considerable overlap between the low-lying conduction bands. Accordingly, the densities of states for $I4_1/amd$ and $P4/mmm$ MBiS$_2$ in the energy region from 0 to 4 eV are more featureless than those for $R\bar{3}m$ and $Fd\bar{3}m$ MBiS$_2$. The differences mentioned above may be understood as follows. For $R\bar{3}m$ and $Fd\bar{3}m$ MBiS$_2$, only the M-S-Bi-S chains exist along all the x, y, and z directions without the M-S-M-S or Bi-S-Bi-S chains. On the other hand, for $I4_1/amd$ and $P4/mmm$ MBiS$_2$, there exist the M-S-M-S and Bi-S-Bi-S chains. The presence of the Bi-S-Bi-S chains increases the overlap between the Bi $6p$ orbitals, thereby increasing the dispersion of the low-lying conduction bands and resulting in the reduction of the band gaps.

From now on, we focus on $R\bar{3}m$ and $Fd\bar{3}m$ MBiS$_2$ because they are the two lowest-energy superstructures and thus expected to be important as the local superstructures related to the disordered cubic phase observed in the previous experimental studies. As mentioned above, $R\bar{3}m$ and $Fd\bar{3}m$ AgBiS$_2$ exhibit relatively large Δ of about 0.5 eV. On the other hand, $R\bar{3}m$ and $Fd\bar{3}m$ NaBiS$_2$ exhibit smaller Δ of about 0.1 eV, indicating that their band gaps are nearly direct. The nearly direct band gap of NaBiS$_2$ is consistent with the result reported by BaQais et al.;[65] as pointed out by the authors, the nearly direct band gap of NaBiS$_2$ is beneficial for photovoltaic applications because it results in strong optical absorption near the absorption edge and long photocarrier life time.

We next compare our calculated band gaps of $R\bar{3}m$ and $Fd\bar{3}m$ MBiS$_2$ with those reported in the previous studies. The experimental band gap of bulk AgBiS$_2$ are 0.9 eV,[26] which is larger by about 0.5 eV than our calculated band gaps of $R\bar{3}m$ and $Fd\bar{3}m$ AgBiS$_2$, 0.26 and 0.46 eV, respectively. The underestimation of our calculated band gaps is due to the well-known deficiency of the GGA. Our calculated band gap of 0.26 eV for $R\bar{3}m$ AgBiS$_2$ is smaller by about 0.2 eV than the GGA band gaps of 0.42-0.46 eV calculated for $P\bar{3}m1$ AgBiS$_2$ reported by the previous theoretical studies.[42,45,47] Viñes et al. calculated the band gap of $P\bar{3}m1$ AgBiS$_2$ using the more accurate hybrid exchange-correlation functional, HSE06, and found the band gap of $P\bar{3}m1$ AgBiS$_2$ to be 1.54 eV, which is about 70% larger than the experimental band gap of 0.9 eV.[42] As for NaBiS$_2$, since there are no experimental studies of its bulk band gap, the experimental band gaps available for comparison are only those for NaBiS$_2$

thin films;[59–65] the measured values of the band gaps of the thin films are ranged from 1.1 to 1.4 eV. Our calculated band gaps of $R\bar{3}m$ and $Fd\bar{3}m$ $NaBiS_2$, 0.92 and 1.23 eV, are not very different from the experimental band gaps of the $NaBiS_2$ thin films. However, this seems incomprehensible when considering the deficiency of the GGA mentioned above. BaQais et al. calculated the band gap of $NaBiS_2$ using the HSE06 functional and found it to be 1.37 eV,[65] which is larger by 0.1-0.4 eV than our calculated GGA band gaps and falls within the range of the experimental band gaps of 1.1-1.4 eV.

In Fig. 4, we show the absorption spectra of $R\bar{3}m$ and $Fd\bar{3}m$ MBiS$_2$ along with those of $CuInSe_2$ for comparison, whose space group is $I\bar{4}2d$. For $R\bar{3}m$ MBiS$_2$ and $CuInSe_2$, we show the absorption spectra for the electric field of light perpendicular and parallel to the c axis, denoted respectively as $E \perp c$ and $E \parallel c$. All the calculated absorption spectra are scissors corrected using the experimental band gaps of 0.9, 1.1, and 1.0 eV for $AgBiS_2$,[26] $NaBiS_2$,[61] and $CuInSe_2$,[1] respectively.

The calculated absorption coefficients of $R\bar{3}m$ and $Fd\bar{3}m$ MBiS$_2$ are both considerably high, of the order of 10^5 cm^{-1}, in the main part of the solar spectrum. Note that they are much higher than the absorption coefficients of $CuInSe_2$, which is one of the highest-performance absorber materials with high absorption coefficients such as CZTS, CdTe, GaAs, and $CH_3NH_3PbI_3$.[83] For both M=Ag and Na, the absorption coefficients of $R\bar{3}m$ MBiS$_2$ are slightly lower than that of $Fd\bar{3}m$ MBiS$_2$. For M=Na, the absorption coefficient of $R\bar{3}m$ $NaBiS_2$ for $E \perp c$ is slightly higher than that for $E \parallel c$. The absorption edges of $R\bar{3}m$ and $Fd\bar{3}m$ $AgBiS_2$ are located at about 1.4 and 1.3 eV, respectively. These values are larger than the scissors-corrected band gap of 0.9 eV by about 0.5 and 0.4 eV for $R\bar{3}m$ and $Fd\bar{3}m$ $AgBiS_2$, respectively. This is consistent with the results mentioned above that the differences between the indirect and direct band gaps, Δ, are 0.58 and 0.46 eV for $R\bar{3}m$ and $Fd\bar{3}m$ $AgBiS_2$, respectively. Also, the absorption edges of $R\bar{3}m$ and $Fd\bar{3}m$ $NaBiS_2$ are located at about 1.2 and 1.3 eV, respectively. These values are larger than the scissors-corrected band gap of 1.1 eV by about 0.1 and 0.2 eV for $R\bar{3}m$ and $Fd\bar{3}m$ $NaBiS_2$, respectively. This is again consistent with the results that Δ are 0.08 and 0.15 eV for $R\bar{3}m$ and $Fd\bar{3}m$ $NaBiS_2$, respectively.

The large absorption coefficients of MBiS$_2$ obtained in this work are consistent with those reported in the previous studies.[31, 37, 40, 42, 45, 64, 65] The experimental absorption coefficients of the $AgBiS_2$ thin films are of the order of 10^5 cm^{-1}.[31, 37, 40] The previous theoretical studies have also shown that the calculated absorption coefficient of $P\bar{3}m1$ $AgBiS_2$ is of the order of 10^5 cm^{-1}.[42, 45] Yang et al. reported that the synthesized nanocrystals of $NaBiS_2$ exhibit strong absorption in the visible to near-infrared range.[64] BaQais et al. have reported that the

calculated absorption coefficients of $NaBiS_2$ is of the order of 10^5 cm^{-1}.[65]

In Fig. 5, we show the SLME calculated for $R\bar{3}m$ and $Fd\bar{3}m$ $MBiS_2$. The SLME is obtained using the calculated absorption coefficients and the differences between the indirect and direct band gaps, Δ, which is 0.58 and 0.46 eV for $R\bar{3}m$ and $Fd\bar{3}m$ $AgBiS_2$, respectively, and 0.08 and 0.15 eV for $R\bar{3}m$ and $Fd\bar{3}m$ $NaBiS_2$, respectively. For both $E \perp c$ and $E \parallel c$, the SLME in the thick-film limit is 15% for both $R\bar{3}m$ and $Fd\bar{3}m$ $AgBiS_2$ while 30% and 27% for $R\bar{3}m$ and $Fd\bar{3}m$ $NaBiS_2$, respectively. The reason why the SLME of $AgBiS_2$ is much lower than that of $NaBiS_2$ is the large Δ of $AgBiS_2$. We confirmed this by setting $\Delta = 0$ in calculating the SLME. The thus calculated SLME in the thick-film limit was found to be 32% for both $R\bar{3}m$ and $Fd\bar{3}m$ $AgBiS_2$ and 33% for both $R\bar{3}m$ and $Fd\bar{3}m$ $NaBiS_2$. As expected, the change in the SLME resulting from setting $\Delta = 0$ found for $AgBiS_2$ is more pronounced than that found for $NaBiS_2$.

It should, however, be noted that the PCE for absorber materials with indirect band gaps may be underestimated when using the SLME as a metric for quantifying the photovoltaic performance, as pointed out by Bercx et al.[84] They found that the calculated SLME for silicon is unrealistically small and concluded that the origin of this underestimation is its very large Δ of about 2.23 eV. The large Δ results in the radiative fraction of the order of 10^{-38}, which is much smaller than 10^{-3}, a reasonable value expected for silicon. Thus, the relatively large value of Δ of about 0.5 eV for $R\bar{3}m$ and $Fd\bar{3}m$ $AgBiS_2$, although not very large compared to that of silicon, may result in the underestimation of the SLME for these materials. It is safer to consider that the SLME in the thick-film limit calculated for $R\bar{3}m$ and $Fd\bar{3}m$ $AgBiS_2$ in this study, 15%, may be a lower bound for the PCE in the ideal conditions assumed in the SLME formulation.

As shown in Fig. 5, the SLME of both $AgBiS_2$ and $NaBiS_2$ reach 90% of its thick-film-limit values at the film thickness of less than 100 nm, reflecting their high absorption coefficients. In particular, only at the film thickness of 50 nm, the SLME of both $R\bar{3}m$ and $Fd\bar{3}m$ $AgBiS_2$ exceed 90% of its thick-film-limit values. Also, at the same film thickness, the SLME of $R\bar{3}m$ and $Fd\bar{3}m$ $NaBiS_2$ are about 70-80 and 90% of its thick-film-limit values, respectively. The behavior of the SLME of $AgBiS_2$ obtained in this work is consistent with the experimental observation by Bernechea et al.[31] They reported that the ultrathin-film solar cells based on the $AgBiS_2$ nanocrystals exhibited a certified PCE of 6.3%. The measured short-circuit current density of 22 mA/cm^2 is significantly high despite that the thickness of the absorber layer is only 35 nm, indicating that the $AgBiS_2$ nanocrystals with such thin active layers can absorb the sunlight strongly.

4. Conclusions

We have studied the structural, electronic, and optical properties of MBiS$_2$ (M=Ag, Na) using the relativistic all-electron calculations based on the density functional theory. As possible local superstructures associated with their disordered cubic phases, we considered $R\bar{3}m$, $Fd\bar{3}m$, $I4_1/amd$, and $P4/mmm$ MBiS$_2$. It was found that the lowest-energy superstructures are those of $R\bar{3}m$ and $Fd\bar{3}m$ for both AgBiS$_2$ and NaBiS$_2$. $R\bar{3}m$ and $Fd\bar{3}m$ MBiS$_2$ are indirect-band-gap semiconductors. The differences between the indirect and direct band gaps, Δ, for $R\bar{3}m$ and $Fd\bar{3}m$ AgBiS$_2$ are about 0.5 eV while those for $R\bar{3}m$ and $Fd\bar{3}m$ NaBiS$_2$ are about 0.1 eV. Using the four-component spinors obtained as the solutions of the Dirac-Kohn-Sham equations, the absorption coefficients of $R\bar{3}m$ and $Fd\bar{3}m$ MBiS$_2$ were calculated within the independent particle approximation combined with a phenomenological approach. It was found that both AgBiS$_2$ and NaBiS$_2$ exhibit high absorption coefficients of the order of 10^5 cm^{-1}. Using the obtained absorption coefficients, the SLME of $R\bar{3}m$ and $Fd\bar{3}m$ MBiS$_2$ was estimated as a metric for quantifying the photovoltaic performance. The SLME in the thick-film-limit values for AgBiS$_2$ is 15%; the small value for AgBiS$_2$ is due to its large Δ of about 0.5 eV. On the other hand, the SLME in the thick-film limit for NaBiS$_2$ is 32%; the large value for NaBiS$_2$ is due to its small Δ of about 0.1 eV. For both AgBiS$_2$ and NaBiS$_2$, the SLME reach 90% of its thick-film limit at the film thickness of less than 100 nm, reflecting their high absorption coefficients.
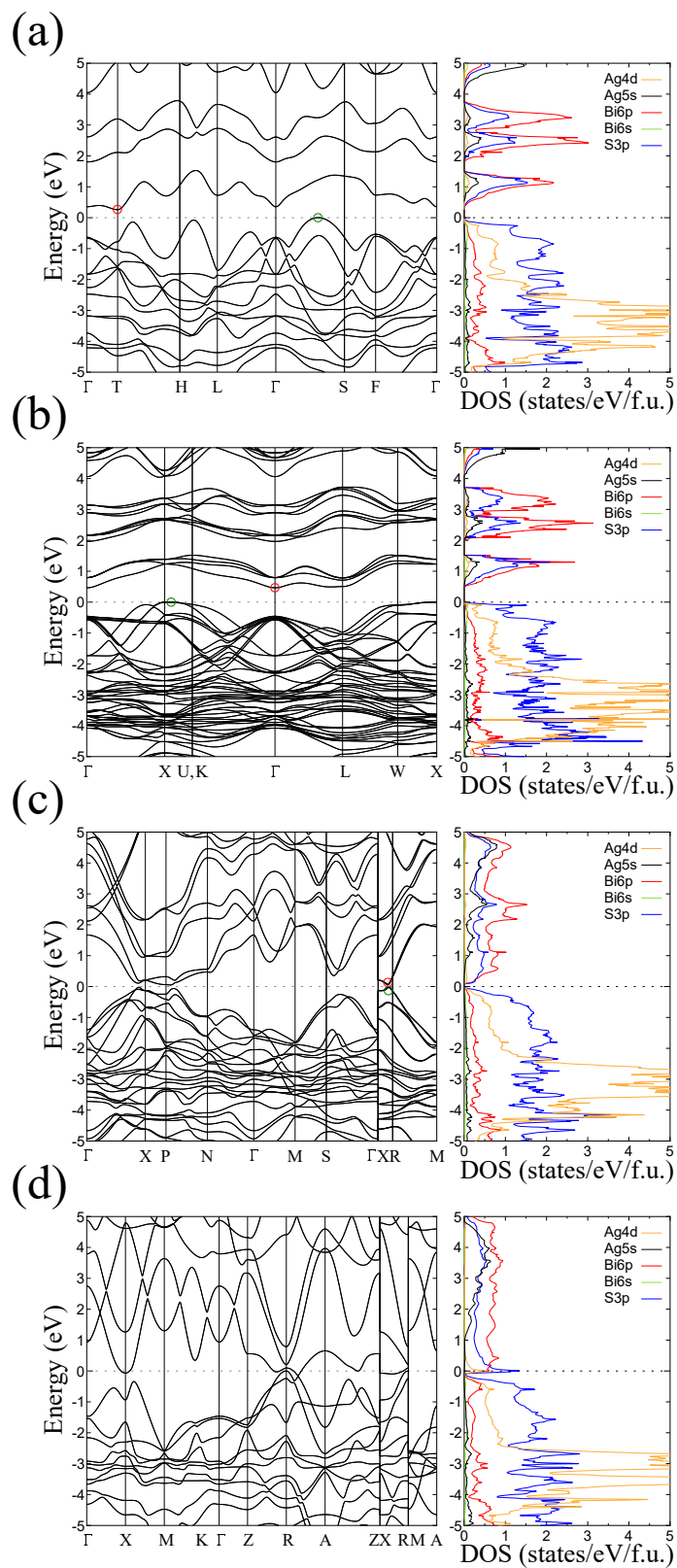
Fig. 2.   (Color online) Band structures and densities of states of (a) $R\bar{3}m$, (b) $Fd\bar{3}m$, (c) $I4_1/amd$, and (d) $P4/mmm$ AgBiS$_2$. The conduction band minimums and the valence band maximums are shown by red and green circles, respectively, except for metallic $P4/mmm$ AgBiS$_2$. The zero of the energy is taken at the top of the valence bands.
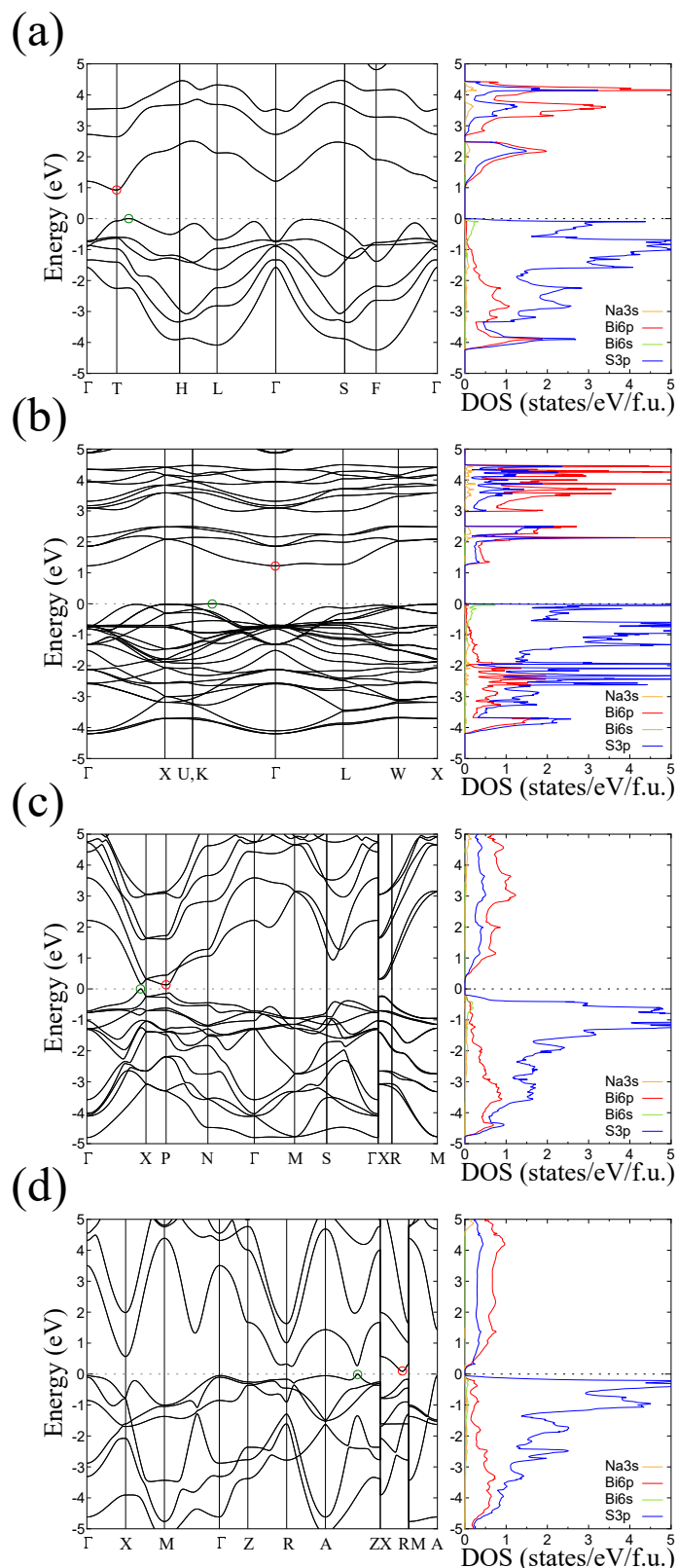
Fig. 3. (Color online) Band structures and densities of states of (a) $R\bar{3}m$, (b) $Fd\bar{3}m$, (c) $I4_1/amd$, and (d) $P4/mmm$ NaBiS$_2$. The conduction band minimums and the valence band maximums are shown by red and green circles, respectively. The zero of the energy is taken at the top of the valence bands.
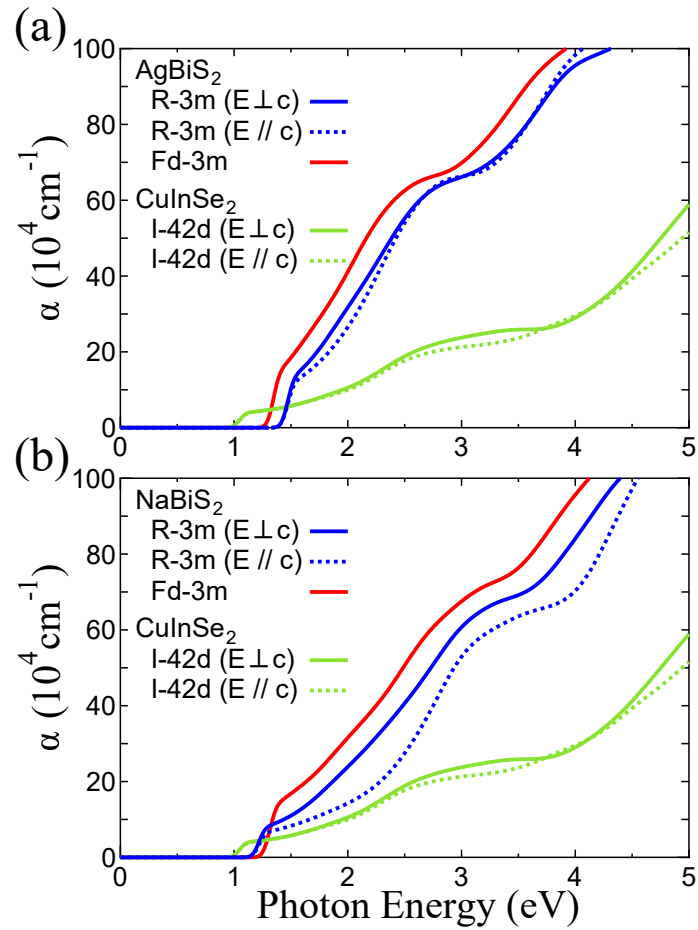
Fig. 4. (Color online) Calculated absorption coefficients α of (a) AgBiS$_2$ and (b) NaBiS$_2$ for the $R\bar{3}m$ and $Fd\bar{3}m$ superstructures. The absorption coefficients for CuInSe$_2$ are also shown for comparison. For the $R\bar{3}m$ superstructure and CuInSe$_2$, the absorption coefficients are shown by solid and dotted curves for the electric field of light perpendicular and parallel to the c axis, respectively. All the calculated absorption spectra are scissors corrected.
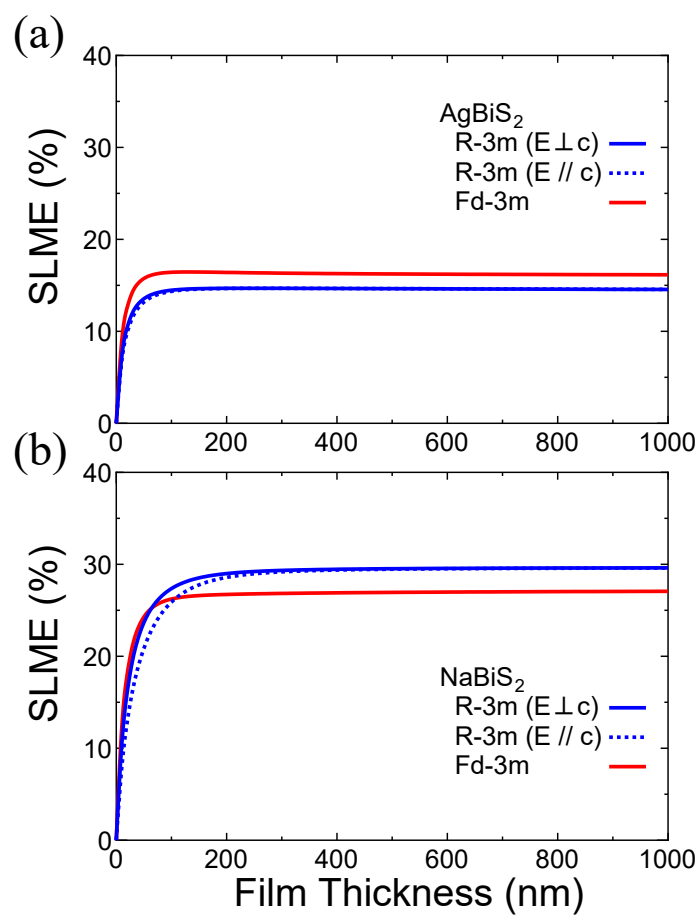
Fig. 5. (Color online) Calculated SLME of (a) AgBiS$_2$ and (b) NaBiS$_2$ as a function of film thickness. For the $R\bar{3}m$ superstructure, the absorption coefficients are shown by solid and dotted curves for the electric field of light perpendicular and parallel to the c axis, respectively.

References

1) T. Feurer, P. Reinhard, E. Avancini, B. Bissig, J. Lockinger, P. Fuchs, R. Carron, T. P. Weiss, J. Perrenoud, S. Stutterheim, S. Buecheler, and A. N. Tiwari, Prog. Photovolt. Res. Appl. **25**, 645 (2017).

2) M. Lingg, S. Buecheler, and A. N. Tiwari, Coatings **9**, 520 (2019).

3) K. Ito and T. Nakazawa, Jpn. J. Appl. Phys. **27**, 2094 (1988).

4) H. Katagiri, K. Saitoh, T. Washio, H. Shinohara, T. Kurumadani, and S. Miyajima, Sol. Energy Mater. Sol. Cells **65**, 141 (2001).

5) H. Katagiri, K. Jimbo, S. Yamada, T. Kamimura, W.-S. Maw, T. Fukano, T. Ito, and T. Motohiro, Appl. Phys. Express **1**, 041201 (2008).

6) H. Katagiri, K. Jimbo, W.-S. Maw, K. Oishi, M. Yamazaki, H. Araki, and A. Takeuchi, Thin Solid Films **517**, 2455 (2009).

7) J. Paier, R. Asahi, A. Nagoya, and Georg Kresse, Phys. Rev. B **79**, 115126 (2009).

8) T. K. Todorov, K. B. Reuter, and D. B. Mitzi, Adv. Mater. **22**, E156 (2010).

9) W. Wang, M. T. Winkler, O. Gunawan, T. Gokmen, T. K. Todorov, Y. Zhu, and D. B. Mitzi, Adv. Energy Mater. **4**, 1301465 (2014).

10) P. Sinsermsuksakul, L. Sun, S. W. Lee, H. H. Park, S. B. Kim, C. Yang, and R. G. Gordon, Adv. Energy Mater. **4**, 1400496 (2014).

11) Y. C. Choi, D. U. Lee, J. H. Noh, E. K. Kim, and S. I. Seok, Adv. Funct. Mater. **24**, 3587 (2014),

12) Y. C. Choi, Y. H. Lee, S. H. Im, J. H. Noh, T. N. Mandal, W. S. Yang, and S. I. Seok, Adv. Energy Mater. 4 1301680 (2014).

13) C. Wu, L. Zhang, H. Ding, H. Ju, X. Jin, X. Wang, C. Zhu, T. Chen, Sol. Energy Mater. Sol. Cells **183**, 52 (2018).

14) L. Whittaker-Brooks, J. Gao, A. K. Hailey, C. R. Thomas, N. Yao, and Y.-L. Loo, J. Mater. Chem. C **3**, 2686 (2015).

15) Z. Li, X. Liang, G. Li, H. Liu, H. Zhang, J. Guo, J. Chen, K Shen, X. San, W. Yu, R. E. I. Schropp, and Y. Mai, Nat. Commun. **10**, 125 (2019).

16) Y. Rodrìguez-Lazcano, M. T. S. Nair, and P. K. Nair, J. Electrochem. Soc. **152**, G635 (2005).

17) A. Kyono and M. Kimata, Am. Mineral. **90**, 162 (2005).

18) C. Garza, S. Shaji, A. Arato, E. P. Tijerina, G. A. Castillo, T. D. Roy, and B. Krishnan, Sol. Energy Mater. Sol. Cells **95**, 2001 (2011).

19) D. J. Temple, A. B. Kehoe, J. P. Allen, G. W. Watson, and D. O. Scanlon, J. Phys. Chem. C **116**, 7334 (2012).

20) M. Kumar and C. Persson, J. Renewable Sustainable Energy **5**, 031616 (2013).

21) M. Kumar and C. Persson, Energy Procedia **44**, 176 (2014).

22) T. Maeda and T. Wada, Thin Solid Films **582**, 401 (2015).

23) S. Banu, S. J. Ahn, S. K. Ahn, K. Yoon, and A. Cho, Sol. Energy Mater. Sol. Cells **151**, 14 (2016).

24) A. W. Welch, L. L. Baranowski, H. Peng, H. Hempel, R. Eichberger, T. Unold, S. Lany, C. Wolden, and A. Zakutayev, Adv. Energy Mater. **7**, 1601935 (2017).

25) Y. Zhang, J. Huang, C. Yan, K. Sun, X. Cui, F. Liu, Z. Liu, X. Zhang, X. Liu, J. A. Stride, M. A. Green, and X. Hao, Prog. Photovolt. Res. Appl. **27**, 37 (2019).

26) B. Pejova, I. Grozdanov, D. Nesheva, and A. Petrova, Chem. Mater. **20**, 2551 (2008).

27) B. Pejova, D. Nesheva, Z. Aneva, and A. Petrova, J. Phys. Chem. C **115**, 37 (2011).

28) S. N. Guin and K. Biswas, Chem. Mater. **25**, 3225 (2013).

29) P.-C. Huang, W.-C. Yang, and M.-W. Lee, J. Phys. Chem. C **117**, 18308 (2013).

30) N. Liang, W. Chen, F. Dai, X. Wu, W. Zhang, Z. Li, J. Shen, S. Huang, Q. He, J. Zai, N. Fang and X. Qian, CrystEngComm **17**, 1902 (2015).

31) M. Bernechea, N. C. Miller, G. Xercavins, D. So, A. Stavrinadis, and G. Konstantatos, Nat. Photonics **10**, 521 (2016).

32) S. N. Guin, S. Banerjee, D. Sanyal, S. K. Pati and K. Biswas, Inorg. Chem. **55**, 6323 (2016).

33) B. Bellal, M. H. Berger, and M. Trari, J. Solid State Chem. **254**, 178 (2017).

34) E. Gu, X. Lin, X. Tang, G. J. Matt, A. Osvet, Y. Hou, S. Jäger, C. Xie, A. Karl, R. Hocke, and C. J. Brabec, J. Mater. Chem. C **6**, 7642 (2018).

35) L. Hu, R. J. Patterson, Z. Zhang, Y. Hu, D. Li, Z. Chen, L. Yuan, Z. L. Teh, Y. Gao, G. J. Conibeer, and S. Huang, J. Mater. Chem. C **6**, 731 (2018).

36) N. Pai, J. Lu, D. C. Senevirathna, A. S. R. Chesman, T. Gengenbach, M. Chatti, U. Bach, P. C. Andrews, L. Spiccia, Y.-B. Cheng, and A. N. Simonov, J. Mater. Chem. C **6**, 2483 (2018).

37) J. van Embden and E. D. Gaspera, ACS Appl. Mater. Interfaces **11**, 16674 (2019).

38) J. C. Calva-Yáñez, O. Pérez-Valdovinos, E. A. Reynoso-Soto, G. Alvarado-Tenorio, O. A. Jaramillo-Quintero, and M. Rincón, J. Phys. D: Appl. Phys. **52**, 125502 (2019).

39) T. Manimozhi, J. Archana, M. Navaneethan, and K. Ramamurthi, Appl. Surf. Sci. **487**, 664 (2019).

40) S. L. Diedenhofen, M. Bernechea, K. M. Felter, F. C. Grozema, and L. D. A. Siebbeles, Sol. RRL **3**, 1900075 (2019).

41) J. T. Oh, S. Y. Bae, S. R. Ha, H. Cho, S. J. Lim, D. W. Boukhvalov, Y. Kim, and H. Choi, Nanoscale **11**, 9633 (2019).

42) F. Viñes, M. Bernechea, G. Konstantatos, and F. Illas, Phys. Rev. B **94**, 235203 (2016).

43) F. Viñes, G. Konstantatos, and F. Illas, Phys. Chem. Chem. Phys. **19**, 27940 (2017).

44) F. Viñes, G. Konstantatos, and F. Illas, J. Phys. Chem. B **122**, 521 (2018).

45) S. Ayhan and G. K. Balcı, Int. Adv. Res. Eng. J. **2**, 1 (2018).

46) P. Ganguly, S. Mathew, L. Clarizia, S. Kumar R, A. Akande, S. Hinder, A. Breen, and S. C. Pillai, Appl. Catal. B **253**, 401 (2019).

47) A. Tabeti, M. Batouche, K. Bidai, A. Djied, T. Seddik, R. Khenata, H. Baltach, and Wang Xiaotian,. Chin. J. Phys. **59**, 578 (2019).

48) L. Mehdaoui, R. Miloua, M. Khadraoui, M. O. Bensaid, D. Abdelkader, F. Chiker, and A. Bouzidi, Physica B **564**, 114 (2019).

49) S. Geller and J. H. Wernick, Acta Crystallogr. **12**, 46 (1959).

50) J. H. Wernick, Am. Mineral. **45**, 591 (1960).

51) A. C. Glatz and A. Pinella, J. Mater. Sci. **3**, 498 (1968).

52) C. Manolikas and J. Spyridelis, Mater. Res. Bull. **12**, 907 (1977).

53) P. Bayliss, Amer. Miner. **76**, 257 (1991).

54) M. Nakamura, H. Nakamura, T. Ohsawa, M. Imura, K. Shimamura, and N. Ohashi, J. Cryst. Growth **411**, 1 (2015).

55) S. Mitra and D. Berardan, Cryst. Res. Technol. **52**, 1700075 (2017).

56) K. Hoang, S. D. Mahanti, J. R. Salvador, and M. G. Kanatzidis, Phys. Rev. Lett. **99**, 156403 (2007).

57) K. Hoang and S. D. Mahanti, J. Sci. Adv. Mater. Dev. **1**, 51 (2016).

58) B. V. Gabrel'yan, A. A. Lavrentiev, I. Ya. Nikiforov, and V. V. Sobolev, J. Struct. Chem. **49**, 788 (2008).

59) S. Kang, Y. Hong, and Y. Jeon, Bull. Korean Chem. Soc. **35**, 1887 (2014).

60) B. A. Rosales, M. A. White, and J. Vela, J. Am. Chem. Soc. **140**, 3736 (2018).

61) J. Guo, Z. Ge, M. Hu, P. Qin, and J. Feng, Phys. Status Solidi RRL **12**, 1800135 (2018).

62) J. Guo, C.-Y. Zhong, Z.-H. Ge, and J. Feng, Phys. Status Solidi A **216**, 1900061 (2019).

63) R. Koutavarapu, G. Lee, B. Babu, K. Yoo, J. Shim, J. Mater. Sci. Mater. Electron. **30**, 10900 (2019).

64) C. Yang, Z. Wang, Y. Wu, Y. Lv, B. Zhou, and W.-H. Zhang, ACS Appl. Energy Mater.

2, 182 (2019).

65) A. BaQais, N. Tymińska, T. L. Bahers, and K. Takanabe, Chem. Mater. **31**, 3211 (2019).

66) T. Zhong, M. Pan, G. Gao, H. Fu, M. Wu, and J.-M. Liu, Phys. Chem. Chem. Phys. **21**, 8553 (2019).

67) J. W. Boon, Rec. Trav. Chim. Pays-Bas **63**, 32 (1944).

68) K. Momma and F. Izumi, J. Appl. Crystallogr. **44**, 1272 (2011).

69) S. Suzuki and K. Nakao, J. Phys. Soc. Jpn. **66**, 3881 (1997).

70) S. Suzuki and K. Nakao, J. Phys. Soc. Jpn. **68**, 1982 (1999).

71) S. Suzuki and K. Nakao, J. Phys. Soc. Jpn. **69**, 532 (2000).

72) M.-F. Li, T. Ariizumi, and S. Suzuki, J. Phys. Soc. Jpn. **76**, 054702 (2007).

73) S. Suzuki and M. Tsuyama, J. Phys. Soc. Jpn. **88**, 075002 (2019).

74) M. Tsuyama and S. Suzuki, J. Phys. Soc. Jpn. **88**, 104802 (2019).

75) S. Suzuki and M. Tsuyama, Jpn. J. Appl. Phys. **58**, 111002 (2019).

76) J. P. Perdew, K. Burke, and M. Ernzerhof, Phys. Rev. Lett. **77**, 3865 (1996).

77) L. Yu and A. Zunger, Phys. Rev. Lett. **108**, 068701 (2012).

78) W. Shockley and H. J. Queisser, J. Appl. Phys. **32**, 510 (1961).

79) "Reference Solar Spectral Irradiance: Air Mass 1.5", https://rredc.nrel.gov/solar//spectra/am1.5/.

80) H. J. Monkhorst and J. D. Pack, Phys. Rev. B **13**, 5188 (1976).

81) L.-K. Hua and Y. Wang, *Applications of Number Theory to Numerical Analysis* (Springer-Verlag, Berlin, 1981).

82) Y. Hinuma, G. Pizzi, Y. Kumagai, F. Oba, and I. Tanaka, Comput. Mater. Sci. **128**, 140 (2017).

83) H. Fujiwara, M. Kato, M. Tamakoshi, T. Miyadera, and M. Chikamatsu, Phys. Status Solidi A **215**, 1700730 (2018).

84) M. Bercx, N. Sarmadian, R. Saniz, B. Partoens, and D. Lamoen, Phys. Chem. Chem. Phys. **18**, 20542 (2016).